

View Article Online
View Journal

Journal of Materials Chemistry B

Materials for biology and medicine

Accepted Manuscript

This article can be cited before page numbers have been issued, to do this please use: K. Kostarelos, D. Despotopoulou, M. Stylianou, L. M. Arellano, T. Kisby and N. Lozano, *J. Mater. Chem. B*, 2025, DOI: 10.1039/D5TB01438G.



This is an Accepted Manuscript, which has been through the Royal Society of Chemistry peer review process and has been accepted for publication.

Accepted Manuscripts are published online shortly after acceptance, before technical editing, formatting and proof reading. Using this free service, authors can make their results available to the community, in citable form, before we publish the edited article. We will replace this Accepted Manuscript with the edited and formatted Advance Article as soon as it is available.

You can find more information about Accepted Manuscripts in the <u>Information for Authors</u>.

Please note that technical editing may introduce minor changes to the text and/or graphics, which may alter content. The journal's standard <u>Terms & Conditions</u> and the <u>Ethical guidelines</u> still apply. In no event shall the Royal Society of Chemistry be held responsible for any errors or omissions in this Accepted Manuscript or any consequences arising from the use of any information it contains.



Engineering of a graphene oxide-based 2D platform of or 1039/D5TB01438G immune activation and modulation

Despoina Despotopoulou^{1,2}, Maria Stylianou^{3,4}, Luis Miguel Arellano¹, Thomas Kisby^{3,4}, Neus Lozano^{1,5}, Kostas Kostarelos^{1,4,5,6*}

- ¹ Nanomedicine Lab, Catalan Institute of Nanoscience and Nanotechnology (ICN2), CSIC and BIST, Campus UAB, 08193 Barcelona, Spain
- ² Departament de Química, Facultat de Ciències, Universitat Autònoma de Barcelona, 08193, Bellaterra, Spain.
- ³ NanoTherapeutics Lab, School of Biological Sciences and Manchester Cancer Research Centre, The University of Manchester, AV Hill Building, Manchester M13 9PT, United Kingdom
- ⁴ Centre for Nanotechnology in Medicine, Faculty of Biology, Medicine & Health, The University of Manchester, Manchester, UK
- ⁵ Institute of Neuroscience, Universitat Autònoma de Barcelona, 08913 Barcelona, Spain
- ⁶ ICREA, Passeig de Lluís Companys 23, 08010 Barcelona, Spain

Correspondence to: kostas.kostarelos@icn2.cat or kostas.kostarelos@manchester.ac.uk

Abstract

Nanoscale-based tools for immunomodulation are expected to offer more targeted and safer approaches to achieve clinically effective manipulation of the local and systemic immune environment. In this study, we aimed to design nanoscale constructs based on graphene oxide (GO) nanosheets as two-dimensional (2D) platform carriers for the TLR7/8 agonist Resiguimod (R848). The physicochemical properties, molecular quantification, as well as proof-of-concept biological activity of the complex were systematically investigated. We hypothesized the formation of the GO:Resiguimod nano-constructs due to the strong π - π interactions between the R848 molecules and the GO surface, and identified that R848 loading efficiency ranged around 75%, quantified by HPLC and UV-Vis. The 2D morphology of the thin nanosheets was retained after complexation, determined by various (AFM and SEM) microscopic techniques. Based on the surface physicochemical characterization of the complexes by Raman, FTIR, XPS, and XRD, the formation of non-covalent interactions among the GO surface and the R848 molecules was confirmed. Most importantly, GO:R848 complexes did not compromise the biological activity of R848, and effectively activated macrophages in vitro. Collectively, thin GO sheets can act as platforms for the non-covalent association with small TLR7/8 agonist molecules, forming stable and highly reproducible complexes, that could be exploited as effective immunomodulatory agents.

Keywords: graphene, nanomedicine, nanoparticle, Resiguimod, immunotherapy

1. Introduction

View Article Online
DOI: 10.1039/D5TB01438G

Immunomodulation encompasses the therapeutic regulation of immune system components through upregulation or downregulation to restore balanced function in response to autoimmune disorders, infections, or malignancies.^{1–4} Despite its potential, immune system modulation achieves therapeutic efficacy in only a subset of patients, highlighting significant clinical limitations.^{5,6} The primary challenges in controlling immunomodulatory mechanisms stem from their inherent complexity, substantial heterogeneity, and the largely uncharacterized dynamic molecular interactions that govern immune network function.^{7–9}

Nanoscale immunomodulatory platforms emerge as promising approaches to achieve targeted and sustained immune system manipulation that favors therapeutic outcomes. ^{10,11} These platforms offer several distinct advantages, including enhanced pharmacokinetic profiles, improved tissue distribution of the immunomodulatory agent(s), and increased cell uptake efficiency. Successful design of precision immunotherapies requires comprehensive characterization of nanomaterial physicochemical properties to enable specific tissue or cellular targeting and optimal antigen presentation. Furthermore, nanoscale delivery systems can enhance therapeutic sustainability by protecting the immunotherapeutic agents from enzymatic degradation while enabling controlled, sustained release or presentation to the immune system. ^{12–15}

Resiquimod (R848), a second-generation and more potent derivative of the FDA-approved imiquimod, belongs to the imidazoquinoline family. Imidazoquinolines are low molecular weight organic compounds with significant antitumor and antiviral features. These features result from their naturally derived, strong immunostimulant properties as they are part of the TLR agonists group. R848 is a double TLR agonist (TLR-7, TLR-8) and binds to specific receptors that are located in the endosome. The mechanism of action involves the activation of pro-inflammatory signalling cascades that result in the secretion of cytokines. PAD-approved imiquimod, and more potential derivative of the FDA-approved imiquimod, and involves the activation of pro-inflammatory signalling cascades that result in the secretion of cytokines.

Imiquimod is clinically approved for the treatment of several skin malignancies or genital warts. On the other hand, several clinical trials have explored the use of R848 as a vaccine adjuvant, or as an antitumor agent against melanoma, cutaneous T-Cell lymphoma or actinic keratosis, yet it has not been approved for any such indication. 20–22 The reason hindering wider clinical acceptance of R848 is primarily linked to its short blood circulation half-life and, more critically, its high off-target toxicity profile. 23,24 Consequently, therapeutic optimization requires implementation of alternative delivery and presentation strategies that enhance both efficacy and safety parameters. 25,26 Nanomaterial-based transport systems offer substantial potential for addressing these limitations through either encapsulation or surface binding of the agonist molecules. Crucially, such approaches should minimize systemic toxicity while preserving its immunomodulatory biological activity. 27,28

2D nanomaterials provide the largest surface area possibly available to enable the facile and robust surface adsorption of immunomodulatory agents, such as R848.²⁹ Graphene oxide (GO) nanosheets additionally offer a variety of surface functionalities providing different types of interactions with the biologically active molecules, good colloidal stability and high dispersibility in biological fluids.^{30,31} Well-described and controlled cytotoxicity profiles on

interaction with a variety of cell types along with the reported biocompatibility and $O_{OI: 10.1039/D5TB01438G}$ biodegradability are promising for the potential adoption of GO as a carrier for immunomodulatory agents. $O_{OI: 10.1039/D5TB01438G}$

In this study, we aimed to take advantage of the above unique combination of properties that GO nanosheets could offer as a carrier and presentation platform of R848 through a facile and highly reproducible non-covalent complexation. We hypothesized that GO and R848 will interact strongly and robustly through π - π interactions and other surface interactions that will lead to stable nano-constructs with immuno-activating capacity. We report on a highly robust and reproducible protocol for the preparation of such GO:R848 nanohybrids, along with their thorough structural and surface characterization. Finally, the biological activity of the GO:R848 complexes is demonstrated using a primary macrophage model to demonstrate their proof-of-concept immunoactivation capacity.

2. Results

2.1. GO nanosheet complex formation with R848.

In this study, the starting materials used for the preparation of the GO:R848 complexes were GO, produced by our group, and the, commercially available, synthetic molecule R848 (**Figure 1A**). The GO material was prepared following the modified Hummers' method under endotoxin-free conditions. The resulting GO nanosheets contained less than 2% of chemical impurities. Also, their average size was below 450 nm as found by Atomic Force Microscopy (AFM) and Scanning Electron Microscopy (SEM) and their thickness was calculated to be 1 nm from the AFM nanosheets' cross-section (**Table S1**). The lateral dimensions and thickness of the GO materials were selected for optimal interaction with the immune cellular component and the maximum surface area available for R848 loading.³⁴ Regarding the immunomodulatory agent, R848 is a synthetic tricyclic organic molecule with a molecular weight of 350.8 g/mol. Its chemical structure consists of an imidazoquinolinamine with two important substitute groups: an ethoxy methyl and a methyl propanol group. For our studies, the hydrochloride analogue of R848 was chosen, as only this form is soluble in aqueous solution (1 mg/mL in water).

Complexes between GO nanosheets and R848 molecules were formed in an aqueous suspension by moderate shaking, as depicted in **Figure 1B**. Briefly, R848 was added to the pH-adjusted GO dispersion (nanosheets at pH 10) and then, the final volume was fixed with water before incubation. Different mass ratios of GO to R848 were tested: 10:10, 10:8, 10:6, and 10:4. The GO:R848 complexes at 10:10 and 10:8 (wt:wt) were colloidally unstable upon mixing of the two components, forming a GO aggregate (**Figure 1C(i)**). On the contrary, complexes with ratios 10:6 and 10:4 (wt:wt) visually formed a stable suspension. To establish the optimal GO:R848 mass ratio, complexes at 10:6 and 10:4 were studied by DLS (**Figure 1C(ii)**) and **Figure 1C(iii)**). No significant changes regarding the ζ-potential were observed for these ratios. Nevertheless, a considerable increase in size distribution was detected at the

This article is licensed under a Creative Commons Attribution-NonCommercial 3.0 Unported Licence

Open Access Article. Published on 24 October 2025. Downloaded on 10/27/2025 10:14:29 AM

The selected GO:R848 complex (10:4) was carefully monitored since the moment of preparation and over 8 days. At day 0, the complex formation was confirmed spectroscopically by UV-Vis (Figure 1D(i) and Figure S1). GO control showed the characteristic peak at 230 nm corresponding to the π - π * transitions of C=C, as well as a shoulder at 300 nm due to $n-\pi^*$ electronic transitions of C=0.35 On the other hand, the observed absorption maxima for R848 control was at 220 and 254 nm with other minor peaks at 310 and 320 nm. The fingerprint features of both pure GO and R848 controls were present in the spectrum of the complex, with a notable increase in the absorbance intensity of GO due to the presence of R848. Moreover, pH monitoring of the complex was followed in each preparation step (Figure 1D(ii)) and over 8 days (Figure 1D(iii)). This monitoring was important as the final pH should fall into the physiological range (7-7.4) for biological applications as well as for ensuring electrostatic stabilization of GO sheets.³⁶ Low pH can cause aggregation driven by the protonation of the carboxyl groups.³⁷ For this reason, the pH of GO sheets was modified from pH 3 to pH 10. This adjustment in a basic pH was necessary, since the subsequent addition of acidic R848 molecules would have reduced the pH out of the physiological range otherwise.

2.2. Purification of GO:R848 complex and quantification of bound R848 molecules.

Following optimization of the suitable ratio to form the GO:R848 complex, a purification process was developed, following 4 ultracentrifugation cycles using 100 kDa membranes for the removal of the unbound R848 molecules (**Figure 2A**).

Before purification of the GO:R848 complexes, GO and R848 controls were tested to validate the purification protocol. For GO and R848 quantification, the calibration curves presented in **Figure S1** were used. Briefly, it was found that 98-100% GO can be quantified by UV-Vis (230 nm) in the purified fraction (material on the filter), and 97-99% of R848 could be quantified by UV-Vis (320 nm) and HPLC (254 nm) in the filtrates, as shown in **Figure S2**, indicating the protocol's suitability for quantification of complexed drug molecules onto the GO.

Subsequently, the loading capacity of R848 onto the GO nanosheets was studied by UV-Vis spectroscopy and HPLC, by measuring the unbound R848 molecules washed through the membrane and collected into the filtrates. The UV-Vis absorption peak intensity for R848 in the filtrates during the purification cycles of the GO:R848 complexes, indicated a descending trend of 9%, 7%, 5% and 2% of R848 in the filtrates F1-F4 respectively. By HPLC these were found to be 12%, 8%, 5% and 2%. Both techniques illustrated the necessity for four centrifugation cycles to achieve removal of unbound R848 (**Figure 2B**). The bound R848, calculated from the measured unbound R848, was found to be between 73-76% by HPLC and UV-Vis (**Figure 2C(i)**). Overall, it was found that for each 1000 µg of GO in the complex, the actual amount of R848 complexed was ca. 300 µg (954 µM).

Open Access Article. Published on 24 October 2025. Downloaded on 10/27/2025 10:14:29 AM.

This article is licensed under a Creative Commons Attribution-NonCommercial 3.0 Unported Licence

In addition, the effect of the purification process onto the GO:R848 complex was explored Article Online Following the ultrafiltration process, the pH of GO and GO:R848 is reduced and remained neutral as was intended due to the removal of any excess sodium hydroxide in the filtrates (Figure 2C(ii)). Also, the purified GO:R848 complex still showed the characteristic peaks of both individual components with an additional reduction in the absorbance intensity in comparison with the unpurified complex. The purified GO:R848 complex absorbance intensity was overall reduced due to the removal of the unbound R848 moieties (Figure 2C(iii)).

2.3. Morphological characterization of the GO:R848 complexes.

The structural features and morphology of the GO:R848 complexes were studied by AFM and SEM. Both were compared to the unmodified GO control. The AFM images showed that the flat morphology and thickness profile of the GO nanosheets was retained after R848 complexation, indicated that drug loading did not provoke any stacking effect (**Figure 3A**). Interestingly, the nanosheet cross-section analysis revealed a uniform height of 0.9 to 1.1 nm, suggesting a complex that consists of 1-2 layers. ³⁸ Moreover, the SEM images showed a smooth lamellae surface, an arrangement which is consistent with the preservation of the typical polygonal morphology of thin GO nanosheets after complexation with R848 (**Figure 3B**). Additionally, lateral size distribution analysis of AFM and SEM data demonstrated that the size range of the complexed nanosheets was very similar to those of GO alone (**Figure S3**). It is worth mentioning that the size reported by SEM and AFM techniques differs from the value that was measured by DLS during the complexes preparation, due to the limitation of the DLS technique in the precise measurement of 2D planar sheets.³⁹

2.4. Spectroscopic, elemental, and structural characterization of GO:R848 complexes.

Detailed characterization was performed using a battery of physicochemical techniques, namely Raman spectroscopy, Fourier transform infrared (FTIR), X-ray photoemission spectroscopy (XPS) and X-ray diffraction (XRD).

The Raman data were collected using a 633 nm laser, and the structural disorder ratio (I_D/I_G) was calculated (**Figure 4A**). It is well known that GO material alone displays typically two peaks: a D band assigned to disordered vibration caused by structural defects, and a G band ascribed to planar stretching of sp²-hybridized carbons at 1327 cm⁻¹ and 1601 cm⁻¹ respectively. A0,41 When complexation with the R848 molecules was performed, it was evident that the spectrum for the GO:R848 complex contained contributions mainly from the GO component. However, new spectroscopic features at around 995, 1473, and 1528 cm⁻¹ ascribed to the imidazoquinoline unit were also detected. Turning our attention to the G band, this mode (1589 cm⁻¹) was downshifted by 12 cm⁻¹ with respect to GO possibly due to the n-doping effect of the R848 as observed in the literature with different electroactive units. Finally, the comparison between the I_D/I_G ratios can provide further information on the materials structure. The I_D/I_G ratio is related to the GO surface oxidation degree and allows for estimation of the degree of defects on the graphitic lattice. A1 In GO:R848 the I_D/I_G ratio was found to be 1.11, slightly lower than for GO starting material (1.24), which may be due to the surface interactions with the R848 and the slight distortion of the GO bands.

However, further techniques were explored to affirm these interactions and their effect of the Conline GO lattice.

Successful complexation of R848 onto GO was also confirmed by interpreting the solid-state FTIR spectrum of the GO:R848 complex compared to the GO control (**Figure 4B**). The infrared spectrum of GO showed the characteristic vibration modes corresponding to the following functional groups; v(C-H) at 2850 cm⁻¹, v(C=O) at 1726 cm⁻¹, v(C=C) at 1625 cm⁻¹, v(O-H) at 1400 cm⁻¹ and v(C-O) at 1046 cm⁻¹. ^{45,46} The GO:R848 complex FTIR data consisted of contributions from both the GO and R848 components. The prominent peak at 1678 cm⁻¹ due to stretching vibration C=N of the imidazole ring, as well as a peak of weak intensity at 750 cm⁻¹ due to the chloride content (since the R848 is a chloride salt), confirmed association of R848 onto the GO surface. ^{47–49} The absence of new vibrational bands in the GO:R848 apart from the individual GO and R848 contributions, affirmed the physical association of the molecule without the formation of any covalent chemical bonds. Finally, the absence of many vibrational bands of R848 in the GO:R848 spectrum may indicate a strong interaction with the GO surface restricting the vibration modes of the organic moieties, as has been previously reported for other molecules with aromatic rings. ^{50,51}

This article is licensed under a Creative Commons Attribution-NonCommercial 3.0 Unported Licence

Open Access Article. Published on 24 October 2025. Downloaded on 10/27/2025 10:14:29 AM.

Additional evidence for GO surface modification was obtained from X-ray photoelectron spectroscopy (XPS) by measuring changes in the elemental composition at the surface of those nanosheets. In general, survey spectra for GO, R848 and GO:R848 exhibited signals corresponding to electrons from the main components C_{1s} , O_{1s} and N_{1s} (Figure 4C(i)). The C_{1s} and O_{1s} peaks appeared in the binding energies of 285 eV and 531 eV respectively. After loading R848, the existence of a novel N_{1s} contribution at a binding energy of around 400 eV was ascribed to the nitrogen content of R848. Atomic percentages from the XPS survey spectra are presented in Figure 4C(ii). In all samples, the detected Si is attributed to the underlying supporting Si substrate used for the measurements. Also, the detected Cl in R848 was around 5%, due to the hydrochloride analogue that was used. Trace elements around 1% of total atomic composition (Cl. S. Mg) may come from impurities during the synthetic procedure. Both for GO and GO:R848, around 60% was C and 30% O, the main two elements of the GO sheets, and around 2-4% Na, due to the neutralization of the GO sheets with sodium hydroxide. Interestingly, a small amount of N (1.2%), which was not present at all in GO, indicated the presence of R848 in the GO sheets and the occurrence of complexation, which could be further confirmed by the N_{1s} high-resolution spectra (Figure **S4A**). Also, the deconvolution of the C_{1s} peak for both the GO control and the GO:R848 complex confirmed the preservation of surface functionalities in the GO material after R848 complexation. This is proved by the absence of significant shift in the peaks corresponding to the functional groups, as depicted in **Figure S4B**. Specifically, the deconvolution of peaks for GO control included the following bonds: C-C and C=C (284.6 eV), C-O (286.7 eV), C=O (287.8 eV), O-C=O (288.7 eV) and π - π * (290.2 eV). Notably, the same peaks were found in the GO:R848 complex in binding energies of 284.6 eV, 286.4 eV, 287.6 eV, 288.7 eV and 290 eV, respectively.

The XRD technique (**Figure 4D**) was used to further interrogate the formation of GO:R848 complexes by comparing the interlayer distance between the nanosheets, as well as possible

Open Access Article. Published on 24 October 2025. Downloaded on 10/27/2025 10:14:29 AM.

BY-NG

This article is licensed under a Creative Commons Attribution-NonCommercial 3.0 Unported Licence

structural disruptions in the case of the GO:R848 complex. In the XRD diffraction patters of STB01438G R848, intense crystalline peaks appeared around 7° and 20° as previously described for imidazoquinoline derivatives. For the GO control, the characteristic peak was obtained as a broad and diffuse signal at $2\theta = 11.59^{\circ}$ with basal spacing of 0.76 nm, as calculated by Bragg's Law. This suggests that GO consists of an amorphous structure which is also retained after R848 complexation. For the GO:R848 complex, the GO peak is shifted to lower 2θ value of 10.02° , which corresponds to a slightly higher basal spacing of 0.88 nm and can be attributed to intercalation of the R848 molecules and a possible rearrangement of the GO nanosheets. As $\frac{1}{2}$ and $\frac{1}{2}$ and $\frac{1}{2}$ are $\frac{1}{2}$ are $\frac{1}{2}$ and $\frac{1}{2}$ are $\frac{1}{2}$ and $\frac{1}{2}$ are $\frac{1}{2}$ are $\frac{1}{2}$ and $\frac{1}{2}$ are $\frac{1}{2}$ and $\frac{1}{2}$ are $\frac{1}{2}$ and $\frac{1}{2}$ are $\frac{1}{2}$ and \frac

2.5. Colloidal stability of GO:R848 complexes.

The colloidal stability of nanomaterial suspensions is an important factor that can be directly influenced by the interactions between the GO nanosheet surface and the nature of the molecule used to form the complex. To evaluate the long-term stability for both the GO and GO:R848 complex aqueous suspensions, their pH, mean particle diameter and ζ -potential were monitored over 2 months. The pH of the GO control and the GO:R848 complexes remained stable (pH~7-8), the size distribution curves (by DLS) ranged between 200-300 nm with a good Gaussian distribution and the ζ-potential fluctuated between -35 and -45 mV, all suggesting maintenance of colloidal stability (Figure S5A and Figure S5B). Interestingly, lack of any R848 detachment from the GO surface within a period of 2 months under storage in dark conditions and at room temperature indicated strong π - π interactions between GO and R848 (Figure S5C). The long-term morphology of the nanosheets was analysed by AFM and SEM (Figure S5D and Figure S5E). No nanosheet stacking or severe morphological changes were observed both for the GO control and the GO:R848 complexes. The thickness of the sheets in both suspensions was found stable between 1-1.2 nm, indicating the high stability of the materials after 2 months. The size distribution data (Figure S3) suggested that the nanosheets were able to preserve their initial structural characteristics and were comparable between the GO alone and its complex with R848.

Lastly, prior to the biological studies, it was necessary to assess the colloidal properties of GO and GO:R848 in the cell culture media (DMEM + 10% FBS) for 24 h. Visually, some clusters formed at 24 h possibly due to the nanosheets' protein coating (**Figure S6A**). Both at 0 h and 24 h, as shown by AFM, the protein association on the GO surface can be observed. However, the typical polygonal morphology of the flakes was retained in all cases, suggesting colloidally stable nanosuspensions that could be further used for the *in vitro* studies (**Figure S6B and Figure S6C**).

2.6. Biological activity of GO:R848 using primary macrophages.

After the formation of the GO:R848 complex, the structural characteristics and the colloidal stability of the suspensions were demonstrated and described in the previous sections, one of the final aspects for investigation was the complex bioactivity. The main question needed to be answered was whether the surface association of R848 onto the GO surface, compromised the biological potency of the immunomodulator. In order to elucidate this, the activity of GO:R848 was investigated in an *in vitro* setting. Murine bone marrow-derived macrophages

(BMDMs) were exposed to the complex for 2 h and this interaction was evaluated of Quis View Article Online Complex for 2 h and this interaction was evaluated of Quis View Article Online Complex for 2 h and this interaction was evaluated of Quis View Article Online Complex for 2 h and this interaction was evaluated of Quis View Article Online Complex for 2 h and this interaction was evaluated of Quis View Article Online Complex for 2 h and this interaction was evaluated of Quis View Article Online Complex for 2 h and this interaction was evaluated of Quis View Article Online Complex for 2 h and this interaction was evaluated of Quis View Article Online Complex for 2 h and this interaction was evaluated of Quis View Article Online Complex for 2 h and this interaction was evaluated of Quis View Article Online Complex for 2 h and this interaction was evaluated of Quis View Article Online Complex for 2 h and 2 known to possess distinct autofluorescence properties enabling tracking and imaging of the interaction with live cells.⁵⁵ Following exposure of BMDMs, both GO and GO:R848 treated cells showed an increased autofluorescence which co-registered with the presence of black particles (attributed to GO) specifically in these cells confirming the interaction of both GO and GO:R848 with the cells (Figure 5A and Figure S7). Subsequently, the biological activity of the complex was investigated by analyzing the immunoactivation of BMDMs by expression of an activation marker CD80. To rule out any contribution of cytotoxicity to the immunological responses, the viability of the BMDMs exposed to GO:R848, R848, or GO at the tested concentrations was first evaluated, and no toxicity was observed (Figure 5B). Flow cytometry analysis demonstrated that GO:R848 could increase the percentage of macrophages (F480+/CD11b+) expressing CD80 to the same levels as free R848, confirming that the R848 biological activity is maintained (Figure 5C and Figure S8). To further validate these results, the production of TNF-α, a key pro-inflammatory cytokine that is released upon activation of macrophages was also assessed. TNF-α levels were significantly upregulated in GO:R848 treated cells compared to the controls including free R848 (Figure **5D**). Overall, these results confirmed that GO:R848 can act as a suitable platform for the delivery of R848 to immune cells while maintaining the immunostimulatory activity, therefore highlighting the potential for future use as an immunotherapeutic nano-construct.

3. Discussion

In this study, a robust protocol for the non-covalent complexation and purification of GO with the immunomodulatory molecule R848 was presented. The GO:R848 complexes showed a drug loading capacity of 75% and a negative surface charge that prevented aggregation. It was shown that the complexed R848 did not bear any significant structural impact on the thickness and lateral dimension of the ensuing nanosheets. Detailed characterization of the complexes using an array of different techniques strongly confirmed the presence and strong interaction of R848 molecules onto the GO surface. Long-term stability studies demonstrated that the complex remained a colloidally stable suspension, without any morphological changes or R848 detachment from the GO surface, further indicating the strong physical interactions between the two complex components. Most importantly, the GO:R848 complex was shown to preserve the immunostimulatory activity of R848 in primary macrophage cultures.

Up to now, limited studies have been published regarding the formation of two-dimensional GO:R848 complexes. A chemically functionalized GO platform with amino-thiophenol crosslinked to polyethylenimine was used for the combined delivery of plasmid DNA (OVA-encoding) and of the immunomodulator R848.⁵⁷ Similarly, Yin et al. designed a hydrogel as cancer nanovaccine that contained GO flakes chemically functionalised with polyethylenimine (PEI) complexing mRNA (OVA-encoding) and the R848 adjuvant.⁵⁸ In addition, Huang et al. developed a GO platform as an adjuvant for influenza vaccine. In this case, graphene quantum dots (modified with carnosine) were complexed with R848 and self-

assembled in the presence of Zn⁺² ions to a micrometer-sized system.⁵⁹ Despite these report Article Online exploring the use of R848 molecules as vaccine adjuvants, no thorough physicochemical characterization of the GO:R848 complex itself has been previously presented. Here we attempted to unravel a method for the generation and characterization of a purified GO:R848 complex using a battery of different structural, surface, elemental and colloidal investigations. It is worth mentioning that throughout these studies, GO alone was used as a control. We intentionally did not introduce any functional groups to the GO surface, hypothesizing that the strong non-covalent interactions between the highly purified and thin GO lattice with the R848 molecules will lead to a stable complex with minimal interference to the surface properties of the nanosheets.

The use of R848 and other immune-modulating molecules in this family has not been greatly explored in combination with 2D materials. Sun et al. used boron nanosheets, prepared by a liquid exfoliation technique from bulk boron, modified with polydopamine and loaded with tumor antigen and R848 in a platform combining immunotherapy and phototherapy. 60 Liao et al., utilized black phosphorus nanoparticles modified with PLGA and loaded with R848 for photothermal therapy against liver cancer. 61 In these reports, R848 was also attached on a polymer-functionalized 2D surface, so clear R848 interactions with the bare 2D surface were not explored. Despite the limited studies using 2D materials, R848 has been successfully encapsulated within a few different types of nanocarriers, including poly(lactic-co-glycolic acid) (PLGA), cyclodextrin, hyaluronic acid polymeric platforms and Au nanoparticles. 62-67 Notably, in the majority of the above, non-covalent association of R848 with the nanocarriers was reported to allow for minimal interference with the R848 inherent chemical and biological properties, since minor modifications of its structure can alter significantly its potency. 68 Our approach in forming the GO:R848 complexes non-covalently was along the same lines, along with sufficient complexation efficiency (around 75% of initial 0.4 mg R848 mass) presumably due to the large surface area on the GO lattice available and the strong π - π interactions between the two components. In specific cases of PLGA (initial 0.8 mg R848 mass) or gold nanoparticles (initial 0.1 mg R848 mass), lower entrapment efficiencies have been reported (around 8% and 30% respectively), maybe due to weaker interactions between the R848 molecules and the carrier nanoparticles. 62,67

On the biological front, concerted efforts need to be made for strategies that overcome the reported systemic toxicity from R848 administration. Among such approaches, the preparation of prodrug formulations, as tocopherol-functionalized R848 loaded into polymeric carriers, or azide-masked R848 have been described.^{69,70} Also, smart responsive nanosystems through hydrolyzable bonds have been designed for specific release of the R848 in targeted areas (e.g lysosomes).^{25,28,71,72} In our approach, emphasis was placed on the adherence and stable complex formation between the nanocarrier and the R848 molecules in order to minimize toxicity risks from free or detached R848. Furthermore, the capability of the GO nanosheets to internalize within immune system components is critical to achieve effective immunomodulatory effects. For example, Li et al. reported targeting of dendritic cells through mannose-functionalization of the nanoparticles.⁷³ We had previously demonstrated the inherent immune cell component affinity of the thin GO nanosheets used in

this study, able to be internalized by macrophages resident in the tumor microenvironment of the GO:R848 Demonstration in this work that such properties can also be preserved for the GO:R848 complex is critical in their exploration as an immunomodulatory platform. Even though most of the previously published work using R848 has been oriented towards cancer immunotherapy via macrophage repolarization, chemoimmunotherapy, or combinations of immunotherapy with phototherapy, 66,74,75 a limited number of reports also describe nanocarrier-based R848 immunomodulation in different applications, such as infections or allergies. 76,77

Overall, R848 has been previously identified as a potent immunoadjuvant for innate immune cell activation, including macrophages and dendritic cells. $^{78-80}$ Delivery and presentation of R848 to these cell types, or to sites where these cell types reside, can improve both immunomodulatory activity and reduce off-target effects. Toward this, we demonstrated that a purified and highly stable GO:R848 nano-construct could interact with and effectively activate macrophages *in vitro*, confirming the preservation of its immunomodulatory capacity. Interestingly, no detectable R848 release was observed from GO:R848 under storage conditions, consistent with strong π – π stacking between R848 and the GO surface. This observation suggests a possible mechanism of R848 engaging TLR7/8 receptors while remaining active and bound to the GO nanosheets, with the intact GO:R848 complex being processed by the macrophages. As this remains a hypothesis, further investigations are warranted to elucidate the exact mechanisms of GO:R848 activity, as well as to investigate whether these complexes can contribute to improved therapeutic effects in the context of a disease model.

4. Conclusion

This investigation has established the effectiveness of thin graphene oxide nanosheets as a two-dimensional (2D) carrier and presentation platform for the immunomodulatory agent R848, which demonstrates significant potential in immunotherapeutic applications. Complex formation between GO and R848 was confirmed through comprehensive characterization using the combination of multiple analytical techniques, revealing robust non-covalent interactions between R848 molecules and the GO lattice. The resulting system exhibits favorable characteristics for further biological use, including sustained chemical and colloidal stability over extended periods and, critically, retention of its bioactivity following complexation. Altogether, this approach illustrates a simple and highly reproducible method for the complexation of R848 onto GO nanosheets aiming at the generation of flat-shaped nano-constructs with immunomodulatory properties. Further studies are warranted to determine the *in vivo* immunomodulatory efficacy of these 2D-shaped nano-constructs and assess their contribution to improved overall immunotherapeutic outcomes.

Open Access Article. Published on 24 October 2025. Downloaded on 10/27/2025 10:14:29 AM. This article is licensed under a Creative Commons Attribution-NonCommercial 3.0 Unported Licence

5. Experimental section

View Article Online DOI: 10.1039/D5TB01438G

Reagents: Endotoxin-free GO was internally provided by our group and was prepared with a modified Hummers' method, as previously described.⁴⁵ Resiquimod (R848) was purchased from InvivoGen (sterile, ≥ 95% HPLC purity). Water for injections (WFI) used for the graphene oxide production and complexes preparation was purchased from Gibco. Additional chemicals used were purchased from Sigma-Aldrich (Merck, Spain). Cell culture reagents were purchased from Sigma-Aldrich (Merck, UK) unless stated otherwise. Amicon Ultra-4 100 kDa MWCO Centrifugal Filter units were purchased from Merck Millipore (UFC810024).

GO:R848 complex preparation: Firstly, R848 powder was resuspended in water for injection to obtain a stock solution of 1 mg/mL and stored at -20°C. GO dispersion was adjusted to a final pH of 10 with 0.1 M sodium hydroxide. The surface association of R848 onto GO was performed by a mild mixing of R848 with the GO sheets in water, at different GO:R848 mass ratios (wt:wt) 10:10, 10:8, 10:6, and 10:4. GO nanosheets at an initial concentration of 1000 μg/mL were mixed with R848 molecules at a certain concentration of 1000, 800, 600, and 400 μg/mL respectively. The overall complexation volume was kept constant at 1 mL by the addition of water. Then, the obtained suspension was incubated under mild shaking conditions (1 G), at room temperature for 30 min, followed by 1 h of stabilization. For the controls, free R848 was diluted at a final concentration of 400 μg/mL. GO control, at a concentration of 1000 μg/mL, followed the same protocol described above, without the step of R848 addition.

GO:R848 complex purification and quantification of bound R848 molecules: For the purification of the complex mixture from any unbound R848 moieties, 100 kDa Amicon Ultra Centrifugal Filter units were used. For that step, the complex 10:4 was centrifuged 4 times at 4000 G, at 20°C for 10 min. After each cycle, the filtrate was collected, and the volume of the purified fraction (on top of the membrane) was adjusted with water for the next round. The same procedure was also followed for the GO control for comparative reasons. Next, the loading amount of R848 on the GO sheets was indirectly calculated by measuring the concentration of unbound R848 present in the collected fractions with UV-Vis spectroscopy and HPLC. The formula used for the calculation of the %bound R848 (drug entrapment efficiency) was the following:

%Bound R848 =
$$\frac{[Initial\ R848] - [Unbound\ R848]}{[Initial\ R848]} \times 100\%$$
 (1),

where [Initial R848]: theoretical R848 concentration mixed with GO (in μ g/mL) and [Unbound R848]: quantified R848 collected in the filtrates after purification (in μ g/mL)

UV-Vis Spectroscopy: GO and R848 samples were diluted in water at concentrations ranging from 2.5 to 20 µg/mL and from 2 to 40 µg/mL respectively and they were measured using a Hellma QS Quartz cuvette. Absorbance spectra were recorded using the Evolution 201 UV-Vis spectrophotometer (Thermo Scientific) in the range of 200-800 nm at room temperature. The standard curves were obtained for GO at 230 nm⁴⁵ and for R848 at 320 nm⁸¹ in above-mentioned concentrations and showed high linearity with a correlation coefficient (R^2) of 0.999. Unloaded R848 was calculated by interpolation from the calibration curve. The spectra were analyzed with Origin software (version b9.5.0.193).

High-Performance Liquid Chromatography: R848 chromatograms were recorded by HPLC system (PerkinElmer Flexar) with a multiwavelength UV-Vis photodetector and a C18 Hypersil BDS column (4.6×150 mm, 5 μm, Thermo Fisher). The chromatographic analysis was carried out using mobile

phase A (0.1% TFA in water) and mobile phase B (0.1% TFA in acetonitrile) following an isocraffe Article Online elution (50:50 v/v) and a flow rate of 1 mL/min. The injection volume was 10 μ L. R848 was detected at 254 nm^{62,69} and the retention time was approximately 2.1 \pm 0.05 min. The standard curve was linear over the concentration of 5 to 100 μ g/mL with a correlation coefficient (R²) of 0.999.

Atomic Force Microscopy: Samples were prepared by covering a cleaved mica surface (Ted Pella) with 20 μ L of 0.01% poly-L-lysine solution (Sigma-Aldrich). After washing with water, 20 μ L of GO dispersion at a concentration of 0.1 mg/mL were drop-casted and washed again with water. For the measurements, the atomic force microscope Asylum MFP-3D (Oxford instruments) was used in airtapping mode. Silicon probes (Ted Pella) with a resonance frequency of 300 kHz and nominal force 40 N/m were used. AFM images of 5×5 μ m were processed with Gwyddion software (version 2.57).

Scanning Electron Microscopy: 20 µL of samples with GO concentrations of 0.1 mg/mL were drop-casted on grids with Ultrathin C on the Lacey C film (Ted Pella) and the excess of the droplet was removed by blotting. The procedure was repeated 4 times and the samples were dried overnight at room temperature. SEM images were recorded at the ICN2 Electron Microscopy Unit with a Magellan 400L field emission microscope (Oxford instruments) and an Everhart-Thornley detector for secondary electrons. The measurement conditions were 100 pA beam current and 20 kV acceleration voltage. The image processing was performed using ImageJ software (version 1.8.0).

Raman Spectroscopy: Samples were prepared by drop-casting 20 μ L of 0.1 mg/mL GO on top of a glass coverslip and then dried overnight at room temperature. A confocal Raman microscope (Witec) under laser excitation of 633 nm and 600 g/mm grating was used for the recording of the measurements. Power of 1 mW for 10 s was used to irradiate the sample and for the focusing an objective lens of 50× magnification was selected. The spectra baseline was corrected and the I_D/I_G ratios were calculated on the maximum of the D and G bands of each sample.

Fourier Transform Infrared Spectroscopy: Samples were prepared on potassium bromide via a casting process. The spectra were collected at the ICN2 Molecular Spectroscopy and Optical Microscopy Facility with a Tensor 27 FT-IR spectrometer (Bruker). A resolution of 4 cm⁻¹, a scan range of 3750 to 600 cm⁻¹ and a baseline correction treatment were selected.

X-ray Photoemission Spectroscopy: 20 μL of the sample were drop-casted several times until a thin film was formed on top of a 5×5 mm Si wafer (Ted Pella). A Phoibos 150 (SPECS, GmbH) electron spectrometer coupled with a hemispherical analyzer, under ultrahigh-vacuum conditions and with an Al Kα (hv=1486.74 eV) X-ray source was used for the measurements acquisition. The measurements were performed at the ICN2 Photoemission Spectroscopy Facility and processed with CasaXPS software. Charge effects were removed by calibrating the C_{1s} line from adventitious carbon at 284.6 eV. For the deconvolution of the C_{1s} peak a Shirley background subtraction was chosen. All the ascribed functional groups were fitted using a Gaussian-Lorentzian function (70:30) except for the group C-C, C=C for which an asymmetric Lorentzian function was preferred. The different peaks were constrained on a full width at half maximum range between 0.5 and 2.5 eV, except the π - π * bond with a range 0-2 eV. Finally, the peak positions were constrained based on NIST's XPS database as follows: C-C and C=C at 285.5-284 eV, C-O at 286.6-285.5 eV, C=O at 287.8-286.8 eV, O=C-O at 290-288.6 eV and π - π * at 292-290 eV.

X-ray Diffraction: 200 μL of the sample was drop-casted on a Si holder and dried in the oven at 50°C. The spectra were collected in the 2θ scan range from 5° to 60° with a diffractometer (Malvern PANalytical X'Pert Pro MPD). For the measurements performed at the ICN2 XRD Facility, the x-ray

This article is licensed under a Creative Commons Attribution-NonCommercial 3.0 Unported Licence

Open Access Article. Published on 24 October 2025. Downloaded on 10/27/2025 10:14:29 AM

source of a ceramic X-ray tube with Cu K α anode (λ =1.540 Å) and the X'Celerator solid-state View Article Online detector were used. The spectra were analyzed with X'Pert HighScore (version 2.2c (2.2.3)) software.

Stability evaluation of GO:R848 complex: For the evaluation of long-term colloidal stability the purified GO:R848 complex and GO control, suspensions were stored at room temperature and in dark conditions. At specific time points, their pH was measured, their colloidal properties were assessed by DLS, and the R848 detachment from the GO surface was investigated.

pH measurements: For the pH measurements, the FiveEasy™ FP20 pH meter equipped with the Mettler Toledo™ pH Electrode InLab Ultra-Micro-ISM was used.

 ζ -potential and hydrodynamic diameter measurements: The ζ -potential and hydrodynamic diameter were measured with a Zetasizer Nano ZS (Malvern Instruments) at the ICN2 Molecular Spectroscopy and Optical Microscopy Facility. 1 mL of samples at a GO concentration of 20 μg/mL were prepared and loaded in disposable capillary cells. The water dispersant settings for viscosity and refractive index were selected and each sample was measured three times at room temperature. The data were analyzed with Zetasizer (version 7.12) software and plotted as mean \pm standard deviation unless stated otherwise.

R848 detachment from GO surface: Drug detachment experiments for the purified complex were performed in specific time points by centrifuging 4 times at 4000 G, 20°C for 10 min, using 100 kDa Amicon Ultra Centrifugal Filter devices. Similar to the purification process, UV-Vis spectroscopy and HPLC were used to determine the amount of R848 collected in each filtrate.

Stability in cell culture medium: GO and GO:R848 were diluted in Dulbecco's Modified Eagle Medium (DMEM) supplemented with 1% Penicillin/Streptomycin and 10% fetal bovine serum (FBS) at a final concentration of 0.1 mg/mL and stored at room temperature. Visual colloidal properties were monitored at 0, 4, 8 and 24 h. Also, AFM analysis was performed at 0 and 24 h.

Bone marrow-derived macrophage cell culture (BMDMs): BMDMs were isolated from fibula and tibias of C57/BL6 female mouse and filtered through a 100 μm cell strainer. Bone marrow cells were then cultured with Dulbecco's modified eagle medium (DMEM) supplemented with 1% L-Glutamine, 1% Penicillin/Streptomycin, 10% fetal bovine serum (FBS) and 10 ng/mL murine-colony stimulating factor (M-CSF) (Peprotech, UK). Cells were cultured in non-treated cell culture dishes (Corning, UK), with 5% CO₂, at 37°C. Medium was refreshed on day 2, 4 and 6 with medium containing M-CSF at a final concentration of 10 ng/mL. Adherent cells were collected post-maturation period, on day 6-7 of differentiation for the *in vitro* experiments.

Flow cytometry: BMDMs were plated in non-treated 24-well plates (Corning, UK) at a ratio of 200,000 cells/well. In parallel, cells were treated with LPS (100 ng/mL) / IFNgamma (20 ng/mL), GO (10 μg/mL), GO:R848 (10 μg/mL:4 μg/mL) and R848 (4 μg/mL) and incubated for 24 h with 5% CO₂, at 37°C. Cells were detached using 10 mM EDTA for 10 min at 4°C and harvested for flow cytometry. BMDMs washed with PBS by centrifugation at 300 G, for 5 min at 8°C and stained with Zombie UV, live/dead (BioLegend, USA) at 1:2000 dilution in PBS, for 15 min at room temperature. Cells were incubated with the conjugated primary antibodies F4/80-APC (1:200), CD11b-BV710 (1:100), CD80-FITC (1:100) and Fc receptor blocker (1:100) for 1 h. Then cells were washed twice with flow buffer (PBS, 2mM EDTA, 2% FBS) at 500 G for 3 min at 8°C and fixed with 1% PFA for 10 min at RT. Finally, cells were resuspended in 200 μL flow buffer and stored in the dark at 4°C until analysis by flow cytometry. Flow cytometry was performed using MCCIR FCF BD LSR Fortessa (BD Biosciences, UK). Flow cytometry analysis was performed using FlowJo software (v10.6.1).

ELISA: BMDMs were plated and treated as described above. Supernatants were collected and TNT workfrice Online ELISA MAX Deluxe Kit (BioLegend, UK), was used to perform ELISA according to manufacturer's protocol.

Live cell imaging: BMDMs were seeded at a density of 100,000/well in CellView 35mm, 4 compartment dishes (Griener Bio-One, UK) and incubated with the treatments stated above for 2 h. Post-treatment, cell supernatant was replaced with DMEM with CellMask green plasma membrane stain (Invitrogen, UK) and live cells were imaged under 5% CO₂ at 37°C, using confocal microscope 710 (ZEISS) with a Primo Plan-ACHTOMAT 40x/oil lens. Images were captured using ZEN 2010 B SP1 software using 594 and 405 lasers with gain of 1115 and 1012, respectively. Microscope settings were kept constant throughout the experiment. ZEN light software (version 9.1.2) was used for the image analysis. Bright field image and GO fluorescence signal images were compared to determine GO uptake and distinguish it from cell autofluorescence.

Statistical analysis: Data analysis and graphical design were performed using GraphPad Prism software (version 6.01). P-values were calculated using two-way ANOVA with Tukey's post-hoc test for multiple comparisons. P-values <0.05 were considered statistically significant. Data are plotted as mean \pm standard deviation unless stated otherwise.

Open Access Article. Published on 24 October 2025. Downloaded on 10/27/2025 10:14:29 AM.

Py-No This article is licensed under a Creative Commons Attribution-NonCommercial 3.0 Unported Licence

Conflicts of interest

View Article Online DOI: 10.1039/D5TB01438G

There are no conflicts of interest to declare.

Author contributions

D.D. performed the main studies including protocol optimization for the complex preparation, physicochemical characterizations and colloidal stability studies. M.A. assisted with the physicochemical characterizations. M.S. and T.K. conducted the *in vitro* experiments and data interpretation. D.D., N.L. and K.K. conceptualized this study and D.D., N.L. and T.K. contributed in the experimental design. K.K. and N.L. supervised, coordinated and maintained funding for this experimental work. D.D. wrote the original version and all authors contributed to the manuscript's writing.

Data availability statement

The data supporting the findings of this study have been included within the article and as part of the Supporting information.

Acknowledgments

The authors would like to thank the European Union Horizon 2020 Research and Innovation Programme under Grant Agreement no. 881603 (Graphene Flagship Core 3) to financially support this project. The ICN2 has been supported by the Severo Ochoa Centres of Excellence programme [SEV-2017-0706] and is currently supported by Grant CEX2021-001214-S funded by MCIN/AEI/10.13039.501100011033. The authors would also like to acknowledge the United Kingdom Research and Innovation (UKRI) Engineering and Physical Sciences Research Council (EPSRC) 2D-Health Programme Grant (EP/P00119X/1). The authors are also thanking Angeliki Karakasidi for the synthesis and characterization of the GO material. Lastly, the authors are acknowledging the ICN2 Advanced Electronic Materials and Devices Group, headed by Prof. Jose A. Garrido for the AFM and Raman measurements that were performed in their laboratory.

References

View Article Online
DOI: 10.1039/D5TB01438G

- K. C. Navegantes, R. Souza Gomes, P. A. T. Pereira, P. G. Czaikoski, C. H. M. Azevedo and M. C. Monteiro, *J. Transl. Med.*, 2017, 15.
- 2 J. Y. Kim, M. G. Rosenberger, S. Chen, C. K. Ip, A. Bahmani, Q. Chen, J. Shen, Y. Tang, A. Wang, E. Kenna, M. Son, S. Tay, A. L. Ferguson and A. P. Esser-Kahn, *ACS Cent. Sci.*, 2023, **9**, 427–439.
- 3 J. Y. Su, W. H. Li and Y. M. Li, Chem. Soc. Rev., 2022, 51, 7944–7970.
- 4 J. Domínguez-Andrés, J. C. Dos Santos, S. Bekkering, W. J. M. Mulder, J. W. M. van der Meer, N. P. Riksen, L. A. B. Joosten and M. G. Netea, *Physiol. Rev.*, 2023, **103**, 313–346.
- 5 M. Sambi, L. Bagheri and M. R. Szewczuk, J. Oncol., 2019, 4508794.
- C. Pilard, M. Ancion, P. Delvenne, G. Jerusalem, P. Hubert and M. Herfs, Br. J. Cancer, 2021, 125, 927– 938.
- 7 B. Pulendran, M.M Davis, Science, 2020, **369**, eaay4014.
- 8 S. P. Kubli, T. Berger, D. V. Araujo, L. L. Siu and T. W. Mak, Nat. Rev. Drug Discov., 2021, 20, 899-919.
- 9 N. Subramanian, P. Torabi-Parizi, R. A. Gottschalk, R. N. Germain and B. Dutta, *Wiley Interdiscip. Rev. Syst. Biol. Med.*, 2015, 7, 13–38.
- 10 D. M. Smith, J. K. Simon and J. R. Baker, Nat. Rev. Immunol., 2013, 13, 592-605.
- 11 W. Sang, Z. Zhang, Y. Dai and X. Chen, Chem. Soc. Rev., 2019, 48, 3771-3810.
- 12 C. W. Shields, L. L. W. Wang, M. A. Evans and S. Mitragotri, Adv. Mater., 2020, 32, 1901633.
- 13 Z. Wang, W. Liu, J. Shi, N. Chen and C. Fan, *Mater. Horizons*, 2018, 5, 344–362.
- 14 H. Liu, X. Shi, D. Wu, F. Kahsay Khshen, L. Deng, A. Dong, W. Wang and J. Zhang, *ACS Appl. Mater. Interfaces*, 2019, 11, 19700–19711.
- 15 J. Deng, J. Wang, J. Shi, H. Li, M. Lu, Z. Fan, Z. Gu and H. Cheng, *Adv. Drug Deliv. Rev.*, 2022, **180**, 114039.
- 16 H. Chi, C. Li, F. S. Zhao, L. Zhang, T. B. Ng, G. Jin and O. Sha, Front. Pharmacol., 2017, 8, 304.
- 17 M. Smith, E. García-Martínez, M. R. Pitter, J. Fucikova, R. Spisek, L. Zitvogel, G. Kroemer and L. Galluzzi, *Oncoimmunology*, 2018, 7, e1526250.
- 18 K. H. Fife, T. C. Meng, D. G. Ferris and P. Liu, Antimicrob. Agents Chemother., 2008, 52, 477-482.
- 19 A. O. Huen and A. H. Rook, Curr. Opin. Oncol., 2014, 26, 237-244.
- 20 G. Frega, Q. Wu, J. Le Naour, E. Vacchelli, L. Galluzzi, G. Kroemer and O. Kepp, *Oncoimmunology*, 2020, 9, 1796002.
- 21 A. H. Rook, J. C. Gelfand, M. Wysocka, A. B. Troxel, B. Benoit, C. Surber, R. Elenitsas, M. A. Buchanan, D. S. Leahy, R. Watanabe, I. R. Kirsch, E. J. Kim and R. A. Clark, *Blood*, 2015, **126**, 2765.
- 22 A. S., Immunotherapy, 2009, 1, 949–964.
- 23 A. L. Engel, G. E. Holt and H. Lu, Expert Rev. Clin. Pharmacol., 2011, 4, 275–289.
- 24 P. J. Pockros, D. Guyader, H. Patton, M. J. Tong, T. Wright, J. G. McHutchison and T. C. Meng, *J. Hepatol.*, 2007, **47**, 174–182.
- 25 H. Kakwere, H. Zhang, E. S. Ingham, M. Nura-Raie, S. K. Tumbale, R. Allen, S. M. Tam, B. Wu, C. Liu, A. Kheirolomoom, B. Z. Fite, A. Ilovitsh, J. S. Lewis and K. W. Ferrara, *Adv. Healthc. Mater.*, 2021, 10, e2100008.
- 26 G. M. Lynn, R. Laga, P. A. Darrah, A. S. Ishizuka, A. J. Balaci, A. E. Dulcey, M. Pechar, R. Pola, M. Y. Gerner, A. Yamamoto, C. R. Buechler, K. M. Quinn, M. G. Smelkinson, O. Vanek, R. Cawood, T. Hills, O. Vasalatiy, K. Kastenmüller, J. R. Francica, L. Stutts, J. K. Tom, K. A. Ryu, A. P. Esser-Kahn, T. Etrych, K.

This article is licensed under a Creative Commons Attribution-NonCommercial 3.0 Unported Licence

Article. Published on 24 October 2025. Downloaded on 10/27/2025 10:14:29 AM

- D. Fisher, L. W. Seymour and R. A. Seder, *Nat. Biotechnol.*, 2015, **33**, 1201–1210.
- View Article Online DOI: 10.1039/D5TB01438G
- 27 C. B. Rodell, S. P. Arlauckas, M. F. Cuccarese, C. S. Garris, R. Li, M. S. Ahmed, R. H. Kohler, M. J. Pittet and R. Weissleder, *Nat. Biomed. Eng.*, 2018, **2**, 578–588.
- 28 J. Wagner, D. Gößl, N. Ustyanovska, M. Xiong, D. Hauser, O. Zhuzhgova, S. Hočevar, B. Taskoparan, L. Poller, S. Datz, H. Engelke, Y. Daali, T. Bein and C. Bourquin, *ACS Nano*, 2021, **15**, 4450–4466.
- 29 B. Ma and A. Bianco, Small, 2021, 17, 2102557.
- 30 J. Liu, L. Cui and D. Losic, Acta Biomater., 2013, 9, 9243-9257.
- 31 D. Bitounis, H. Ali-Boucetta, B. H. Hong, D. H. Min and K. Kostarelos, Adv. Mater., 2013, 25, 2258–2268.
- 32 C. J. Bullock and C. Bussy, Adv. Mater. Interfaces, 2019, 6, 1900229.
- 33 L. Newman, D. A. Jasim, E. Prestat, N. Lozano, I. De Lazaro, Y. Nam, B. M. Assas, J. Pennock, S. J. Haigh, C. Bussy and K. Kostarelos, *ACS Nano*, 2020, **14**, 10168–10186.
- 34 C. Hoyle, J. Rivers-Auty, E. Lemarchand, S. Vranic, E. Wang, M. Buggio, N. J. Rothwell, S. M. Allan, K. Kostarelos and D. Brough, *ACS Nano*, 2018, **12**, 11949–11962.
- 35 P. V. Kumar, N. M. Bardhan, S. Tongay, J. Wu, A. M. Belcher and J. C. Grossman, *Nat. Chem.*, 2014, **6**, 151–158.
- 36 L. Gaohua, X. Miao and L. Dou, Expert Opin. Drug Metab. Toxicol., 2021, 17, 1103-1124.
- 37 C. J. Shih, S. Lin, R. Sharma, M. S. Strano and D. Blankschtein, Langmuir, 2012, 28, 235-241.
- 38 S. Stankovich, D. A. Dikin, G. H. B. Dommett, K. M. Kohlhaas, E. J. Zimney, E. A. Stach, R. D. Piner, S. B. T. Nguyen and R. S. Ruoff, *Nature*, 2006, **442**, 282–286.
- 39 S. A. Sydlik, S. Jhunjhunwala, M. J. Webber, D. G. Anderson and R. Langer, ACS Nano, 2015, 9, 3866–3874.
- 40 D. López-Díaz, M. López Holgado, J. L. García-Fierro and M. M. Velázquez, J. Phys. Chem. C, 2017, 121, 20489–20497.
- 41 A. C. Ferrari, J. C. Meyer, V. Scardaci, C. Casiraghi, M. Lazzeri, F. Mauri, S. Piscanec, D. Jiang, K. S. Novoselov, S. Roth and A. K. Geim, *Phys. Rev. Lett.*, 2006, **97**, 187401.
- 42 M. J. Alvarez-Figueroa, D. Narváez-Araya, N. Armijo-Escalona, E. A. Carrasco-Flores and J. V. González-Aramundiz, *Pharm. Res.*, 2020, **37**.
- 43 X. Dong, D. Fu, W. Fang, Y. Shi, P. Chen and L. J. Li, Small, 2009, 5, 1422-1426.
- 44 C. Casiraghi, A. Hartschuh, H. Qian, S. Pliscanec, C. Georgia, A. Fasoli, K. S. Novoselov, D. M. Basko and A. C. Ferrari, *Nano Lett.*, 2009, **9**, 1433–1441.
- 45 A. F. Rodrigues, L. Newman, N. Lozano, S. P. Mukherjee, B. Fadeel, C. Bussy and K. Kostarelos, *2D Mater.*, 2018, **5**, 035020.
- 46 C. Xu, X. Shi, A. Ji, L. Shi, C. Zhou and Y. Cui, PLoS One, 2015, 10, e0144842.
- 47 M. Afzali, A. Mostafavi and T. Shamspur, Biosens. Bioelectron., 2019, 143, 111620.
- 48 A. Hariharan, M. Kesava, M. Alagar, K. Dinakaran and K. Subramanian, *Polym. Adv. Technol.*, 2018, 29, 355–363.
- 49 L. G. Camargo, P. de Freitas Rosa Remiro, G. S. Rezende, S. Di Carla Santos, M. Franz-Montan and Â. M. Moraes, *Eur. Polym. J.*, 2021, **151**, 110422.
- 50 H. N. Abdelhamid and K. H. Hussein, Biointerface Res. Appl. Chem., 2021, 11, 14726–14735.
- 51 G. F. Wang, H. Qin, X. Gao, Y. Cao, W. Wang, F. C. Wang, H. A. Wu, H. P. Cong and S. H. Yu, *Chem*, 2018, **4**, 896–910.
- 52 W. Yin, D. Xuan, H. Wang, M. Zhou, B. Deng, F. Ma, Y. Lu and J. Zhang, ACS Appl. bio Mater., 2022, 5,

This article is licensed under a Creative Commons Attribution-NonCommercial 3.0 Unported Licence

Downloaded on

Article. Published on 24 October 2025.

View Article Online DOI: 10.1039/D5TB01438G

- 53 S. Park, J. An, J. R. Potts, A. Velamakanni, S. Murali and R. S. Ruoff, Carbon N. Y., 2011, 49, 3019–3023.
- 54 I. de Lázaro, P. Sharp, C. Gurcan, A. Ceylan, M. Stylianou, T. Kisby, Y. Chen, S. Vranic, K. Barr, H. Taheri, A. Ozen, C. Bussy, A. Yilmazer and K. Kostarelos, *Adv. Ther.*, 2021, **4**, 1–15.
- 55 S. Vranic, A. F. Rodrigues, M. Buggio, L. Newman, M. R. H. White, D. G. Spiller, C. Bussy and K. Kostarelos, *ACS Nano*, 2018, **12**, 1373–1389.
- 56 L. J. Cote, F. Kim and J. Huang, J. Am. Chem. Soc., 2009, 131, 1043-1049.
- 57 Y. Yin, T. L. Nguyen, B. Wang, H. T. T. Duong, D. S. Lee, J. H. Kim, J. Kim and J. H. Jeong, *J. Ind. Eng. Chem.*, 2019, **80**, 870–876.
- 58 Y. Yin, X. Li, H. Ma, J. Zhang, D. Yu, R. Zhao, S. Yu, G. Nie and H. Wang, *Nano Lett.*, 2021, **21**, 2224–2231.
- 59 S. Huang, Y. Li, S. Zhang, Y. Chen, W. Su, D. J. Sanchez, J. D. H. Mai, X. Zhi, H. Chen and X. Ding, *J. Control. Release*, 2024, **365**, 716–728.
- 60 Z. Sun, T. Fan, Q. Liu, L. Huang, W. Hu, L. Shi, Z. Wu, Q. Yang, L. Liu and H. Zhang, *Nanophotonics*, 2021, **10**, 2519–2535.
- 61 K. Liao, S. Chen, G. Yang, X. Huang, T. Wang, S. Long, J. Wang, L. Yin, Q. Zou, Q. Liu and Z. Guo, *Heliyon*, 2024, **10**, e27234.
- 62 W. Lin, C. Li, N. Xu, M. Watanabe, R. Xue, A. Xu, M. Araki, R. Sun, C. Liu, Y. Nasu and P. Huang, *Int. J. Nanomedicine*, 2021, **16**, 2775–2787.
- 63 B. Wei, J. Pan, R. Yuan, B. Shao, Y. Wang, X. Guo and S. Zhou, Nano Lett., 2021, 21, 4231–4240.
- 64 W. R. Rodell CB, Arlauckas SP, Cuccarese MF, Garris CS, Li R, Ahmed MS, Kohler RH, Pittet MJ, *Nat. Biomed Eng*, 2018, **2**, 578–588.
- 65 V. Turco, K. Pfleiderer, J. Hunger, N. K. Horvat, K. Karimian-Jazi, K. Schregel, M. Fischer, G. Brugnara, K. Jähne, V. Sturm, Y. Streibel, D. Nguyen, S. Altamura, D. A. Agardy, S. S. Soni, A. Alsasa, T. Bunse, M. Schlesner, M. U. Muckenthaler, R. Weissleder, W. Wick, S. Heiland, P. Vollmuth, M. Bendszus, C. B. Rodell, M. O. Breckwoldt and M. Platten, *Nat. Commun.*, 2023, 14, 771.
- 66 Y. Zhang, T. Yuan, Z. Li, C. Luo, Y. Wu, J. Zhang, X. Zhang and W. Fan, ACS Biomater. Sci. Eng., 2021, 7, 1515–1525.
- 67 I. Mottas, A. Bekdemir, A. Cereghetti, L. Spagnuolo, Y. S. S. Yang, M. Müller, D. J. Irvine, F. Stellacci and C. Bourquin, *Biomaterials*, 2019, **190–191**, 111–120.
- 68 Z. Wang, Y. Gao, L. He, S. Sun, T. Xia, L. Hu, L. Yao, L. Wang, D. Li, H. Shi and X. Liao, *J. Med. Chem.*, 2021, **64**, 7507–7532.
- 69 R. Lu, C. Groer, P. A. Kleindl, K. R. Moulder, A. Huang, J. R. Hunt, S. Cai, D. J. Aires, C. Berkland and M. L. Forrest, *J. Control. Release*, 2019, **306**, 165–176.
- 70 J. Sun, Z. Liu, H. Yao, H. Zhang, M. Zheng, N. Shen, J. Cheng, Z. Tang and X. Chen, Adv. Mater., 2023, 35, 2207733.
- 71 W. Wang, Q. Zhu, Y. Jin, J. Gao, J. Li, X. Zheng, W. Gao, M. Saeed, W. Sheng and H. Yu, *Adv. Healthc. Mater.*, 2023, 12, 2300524.
- 72 S. Chen, Y. Lv, Y. Wang, D. Kong, J. Xia, J. Li and Q. Zhou, ACS Biomater. Sci. Eng., 2023, 9, 773–783.
- 73 Y. Li, Y. Luo, L. Hou, Z. Huang, Y. Wang and S. Zhou, Adv. Healthc. Mater., 2023, 12, 2202871.
- 74 C. G. Da Silva, M. G. M. Camps, T. M. W. Y. Li, A. B. Chan, F. Ossendorp and L. J. Cruz, *Biomaterials*, 2019, 220, 119417.
- 75 Q. Lu, S. Qi, P. Li, L. Yang, S. Yang, Y. Wang, Y. Cheng, Y. Song, S. Wang, F. Tan and N. Li, *J. Mater. Chem. B*, 2019, 7, 2499–2511.

- 76 A. Katebi, R. Varshochian, F. Riazi-Rad, M. Ganjalikhani-Hakemi and S. Ajdary, *Biomed. Pharmacothery* Article Online 2021, **137**, 111276.
- 77 J. Hong, X. Xiao, Q. Gao, S. Li, B. Jiang, X. Sun, P. Ran and P. Yang, *Int. J. Nanomedicine*, 2019, **14**, 7053–7064.
- 78 M. Lee, C. S. Park, Y. R. Lee, S. A. Im, S. Song and C. K. Lee, Arch. Pharm. Res., 2014, 37, 1234–1240.
- 79 X. D. Tang, K. L. Lü, J. Yu, H. J. Du, C. Q. Fan and L. Chen, Cancer Immunol. Immunother., 2022, 71, 2969-2983.
- 80 J. Zhou, Y. Xu, G. Wang, T. Mei, H. Yang and Y. Liu, Int. J. Oncol., 2022, 61.
- 81 D. Paßlick, J. Reinholz, J. Simon, K. Piradashvili, S. Jiang, M. Li, K. Landfester and V. Mailänder, *Nanomedicine*, 2020, 15, 2053–2069.

View Article Online

DOI: 10.1039/D5TB01438G

Figure Legends

Figure 1. Non-covalent complexation of GO:R848 and construct stability.

(A) Component material analysis of the GO:R848 system. GO nanosheets synthesized with the modified Hummers' method shown by AFM and SEM (scale bars 1 μ m) and chemical structure and molecular characteristics of R848 molecules. (B) Schematic of the non-covalent complexation between GO nanosheets and R848 molecules following four sequential steps of reagent addition and a final incubation/mixing step. Note that at the end of this protocol both adsorbed and unbound R848 molecules will be present. (C) Selection of optimal mass (weight) ratio for GO:R848 complex. (i) Visual aspect of GO:R848 complexes at different mass (weight) ratios ranging from 10:10 to 10:4, in comparison to GO control. GO control underwent the same protocol but without the addition of R848; (ii) Average particle surface charge (ζ -potential) of two GO:R848 complexes at mass ratios 10:6 (blue) and 10:4 (red) in comparison to GO control (black); (iii) Mean particle size data by DLS over 8 days at room temperature. Triplicate measurements of at least n=2 sample replicates are shown. (GO (20 μ g/mL); GO:R848 (20 μ g/mL:8 μ g/mL)). (D) Monitoring of GO:R848 complex formation. (i) UV-Vis spectroscopic signal of R848 (green) and GO control (black) compared to the optimal GO:R848 (10:4) complex spectrum (red) at day 0. (GO (20 μ g/mL); GO:R848 (20 μ g/mL:8 μ g/mL); and R848 (8 μ g/mL)); (ii) pH monitoring for GO control (black) and for the GO:R848 complex 10:4 (red) across the different steps of complexation (a-e), as shown in (B); (iii) pH variation over 8 days at room temperature for GO control and GO:R848 complex (10:4); Data expressed as mean \pm SD of at least n=2 sample replicates. Schematic created with BioRender.com

Figure 2. Purification and quantification of bound R848 in the GO:R848 complex.

(A) Schematic depiction of the purification protocol by using column ultracentrifugation. The final GO:R848 complex after purification ('GO:R848 (ap)') was further used for the full physicochemical characterization, while the filtrates F1-F4 (containing any unbound R848 molecules) were used for quantification by UV-Vis and HPLC spectroscopy. (B) Quantification of unbound R848 in the GO:R848 (10:4) complex. (i) UV-Vis spectra of GO:R848 filtrates F1-F4 (unbound R848) in the range of 290-340 nm; (ii) HPLC chromatogram of GO:R848 filtrates F1-F4; (iii) % percentage of R848 after GO:R848 complex purification in the filtrates F1-F4 assessed by UV-Vis and HPLC methods. The results (generated by applying the formula (1) shown in the experimental section) are expressed as mean \pm SD of n=3 replicates. (C) Effect of purification method on the GO:R848 (10:4) complex. (i) Percent (% of originally added) of unbound R848 (green) and bound R848 to the GO surface (brown) as measured by both quantification techniques (UV-Vis and HPLC). The results (generated by applying the formula (1)) are expressed as mean \pm SD of n=3 replicates; (ii) pH monitoring at different steps of purification: GO control (black) and GO:R848 complex (red) before (bp) and after (ap) purification appeared in dashed and solid bars respectively, and their corresponding filtrates (F1-F4) during the purification steps. Data are expressed as mean \pm SD of at least n=3; (iii) UV-Vis spectra of the GO control (black) and the GO:R848 complex (red) capturing the signal before (bp) (dashed line) and after (ap) purification (solid line) in the range 200-800 nm (GO (20 μ g/mL)); GO:R848 (20 μ g/mL)). Schematic created with BioRender.com.

Figure 3. Morphological characterization of GO:R848 complex after purification (ap) by AFM and SEM.
(A) AFM height images with corresponding nanosheet cross-section and thickness graphs (shown underneath) of: (i) GO control; and (ii) GO:R848 complex. (B) SEM micrographs of: (i) GO control; and (ii) GO:R848 complex. In all images scale bars are 1 μm.

Figure 4. Spectroscopic, elemental, and structural characterization of GO:R848 complex after purification (ap). For comparative reasons, the data for GO alone (black) and R848 alone (green) controls are also presented. (A) Raman spectra with the I_D and I_G bands underlined. The I_D/I_G ratios are noted. (B) FTIR spectra with the contribution of the characteristic surface functionality included. (C) (i) XPS high-resolution spectra with characteristic peaks of C_{1s} , O_{1s} , N_{1s} highlighted in the range of 1100-0 eV (CPS is counts per second); and (ii) Total contribution of various functional groups in relative atomic percentages (%) as measured by XPS. Note that Si contribution derives from the Si substrate used during measurement. (D) XRD patterns with the corresponding interlayer distance highlighted. Peak intensities were generally normalized by dividing with the highest value.

Figure 5. Biological activity of the GO:R848 complex demonstrated by effective activation of primary macrophages in vitro.

(A) Interaction of GO and GO:R848 complex with primary bone marrow-derived macrophage (BMDMs) membranes, 2 h post-treatment. Cells were stained with green plasma membrane dye. Bright field confirmed the presence of GO (black particles in bright field). GO autofluorescence (red channel) was used to detect GO-BMDMs co-localization and distinguish it from cell autofluorescence. All images were obtained with confocal microscopy at 40x magnification, zoom factor 2, scale bar 20 μ m. (B) Percentage of viable BMDMs relative to the untreated group, assessed 24 h post-treatment with LPS (100 ng/mL); IFN γ (20 ng/mL), GO (10 μ g/mL), GO:R848 (10 μ g/mL:4 μ g/mL) and R848 (4 μ g/mL), n= 3 biological replicates per condition. (C) Percentage of CD80 (activation marker) out of F480+ CD11b+ cells, 24 h post-treatment under the same conditions. (D) TNF-a expression (pg/ml) of BMDMs supernatant, 24 h post-treatment as mentioned above; n= 6 biological replicates per condition. Data are presented as mean ± SD. Ordinary one-way ANOVA, Tukey's multiple comparisons test (*p \leq 0.05, ** p \leq 0.01, ***p \leq 0.001, ****p \leq 0.0001).

This article is licensed under a Creative Commons Attribution-NonCommercial 3.0 Unported Licence.

Open Access Article. Published on 24 October 2025. Downloaded on 10/27/2025 10:14:29 AM.

FIGURE 1

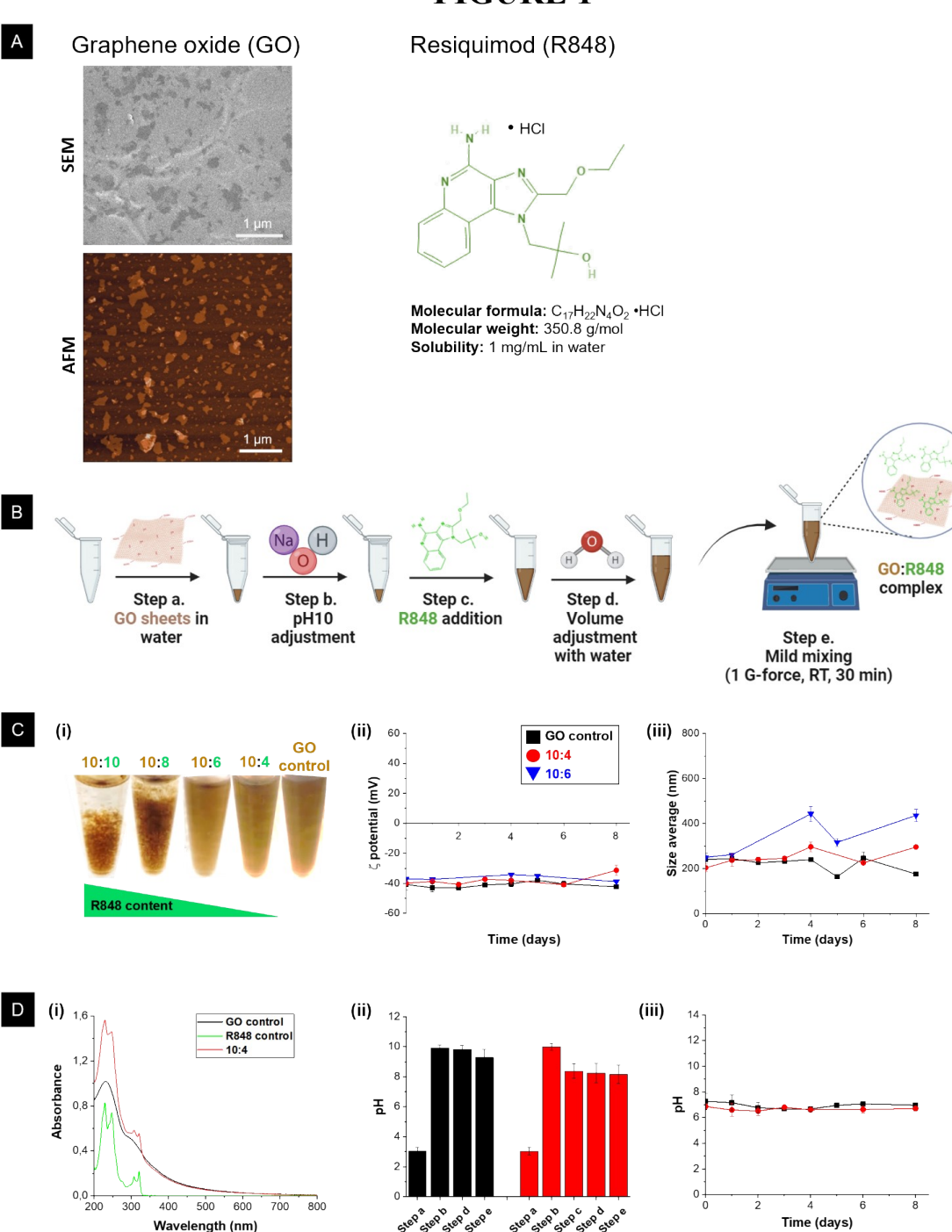


Figure 1. Non-covalent complexation of GO:R848 and construct stability.

(A) Component material analysis of the GO:R848 system. GO nanosheets synthesized with the modified Hummers' method shown by AFM and SEM (scale bars 1 μ m) and chemical structure and molecular characteristics of R848 molecules. (B) Schematic of the non-covalent complexation between GO nanosheets and R848 molecules following four sequential steps of reagent addition and a final incubation/mixing step. Note that at the end of this protocol both adsorbed and unbound R848 molecules will be present. (C) Selection of optimal mass (weight) ratio for GO:R848 complex. (i) Visual aspect of GO:R848 complexes at different mass (weight) ratios ranging from 10:10 to 10:4, in comparison to GO control. GO control underwent the same protocol but without the addition of R848; (ii) Average particle surface charge (ζ -potential) of two GO:R848 complexes at mass ratios 10:6 (blue) and 10:4 (red) in comparison to GO control (black); (iii) Mean particle size data by DLS over 8 days at room temperature. Triplicate measurements of at least n=2 sample replicates are shown. (GO (20 μ g/mL); GO:R848 (20 μ g/mL:8 μ g/mL and 20 μ g/mL:12 μ g/mL)). (D) Monitoring of GO:R848 complex formation. (i) UV-Vis spectroscopic signal of R848 (green) and GO control (black) compared to the optimal GO:R848 (10:4) complex spectrum (red) at day 0. (GO (20 μ g/mL); GO:R848 (20 μ g/mL); and R848 (8 μ g/mL)); (ii) pH monitoring for GO control (black) and for the GO:R848 complex 10:4 (red) across the different steps of complexation (a-e), as shown in (B); (iii) pH variation over 8 days at room temperature for GO control and GO:R848 complex (10:4); Data expressed as mean \pm SD of at least n=2 sample replicates. Schematic created with BioRender.com

FIGURE 2

Journal of Materials Chemistry B

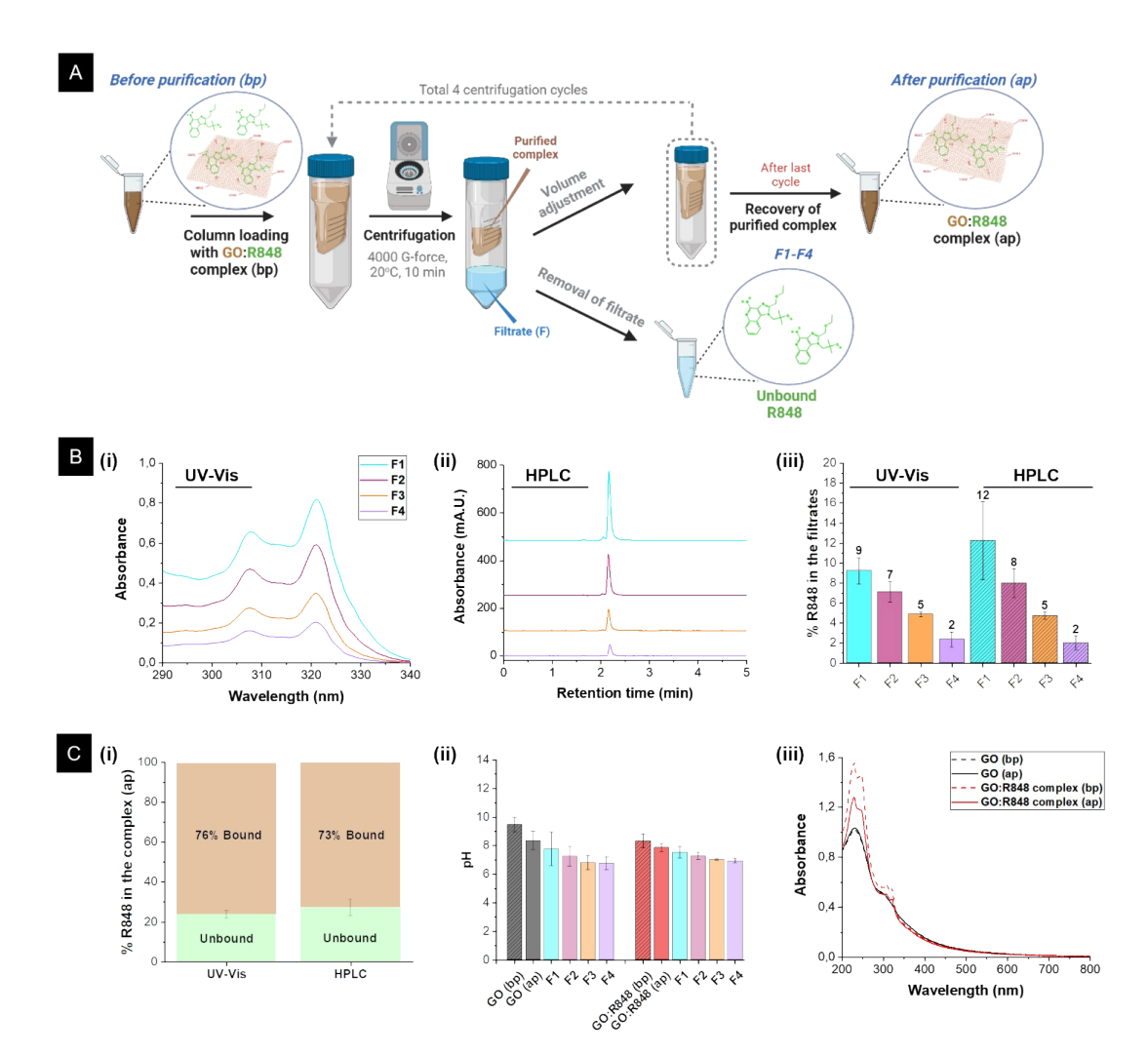


Figure 2. Purification and quantification of bound R848 in the GO:R848 complex.

This article is licensed under a Creative Commons Attribution-NonCommercial 3.0 Unported Licence.

Open Access Article. Published on 24 October 2025. Downloaded on 10/27/2025 10:14:29 AM.

(A) Schematic depiction of the purification protocol by using column ultracentrifugation. The final GO:R848 complex after purification ('GO:R848 (ap)') was further used for the full physicochemical characterization, while the filtrates F1-F4 (containing any unbound R848 molecules) were used for quantification by UV-Vis and HPLC spectroscopy. (B) Quantification of unbound R848 in the GO:R848 (10:4) complex. (i) UV-Vis spectra of GO:R848 filtrates F1-F4 (unbound R848) in the range of 290-340 nm; (ii) HPLC chromatogram of GO:R848 filtrates F1-F4; (iii) % percentage of R848 after GO:R848 complex purification in the filtrates F1-F4 assessed by UV-Vis and HPLC methods. The results (generated by applying the formula (1) shown in the experimental section) are expressed as mean ± SD of n=3 replicates. (C) Effect of purification method on the GO:R848 (10:4) complex. (i) Percent (% of originally added) of unbound R848 (green) and bound R848 to the GO surface (brown) as measured by both quantification techniques (UV-Vis and HPLC). The results (generated by applying the formula (1)) are expressed as mean ± SD of n=3 replicates; (ii) pH monitoring at different steps of purification: GO control (black) and GO:R848 complex (red) before (bp) and after (ap) purification appeared in dashed and solid bars respectively, and their corresponding filtrates (F1-F4) during the purification steps. Data are expressed as mean ± SD of at least n=3; (iii) UV-Vis spectra of the GO control (black) and the GO:R848 complex (red) capturing the signal before (bp) (dashed line) and after (ap) purification (solid line) in the range 200-800 nm (GO (20 μg/mL)); GO:R848 (20 μg/mL: 8 μg/mL)). Schematic created with BioRender.com.

This article is licensed under a Creative Commons Attribution-NonCommercial 3.0 Unported Licence.

Open Access Article. Published on 24 October 2025. Downloaded on 10/27/2025 10:14:29 AM.

FIGURE 3

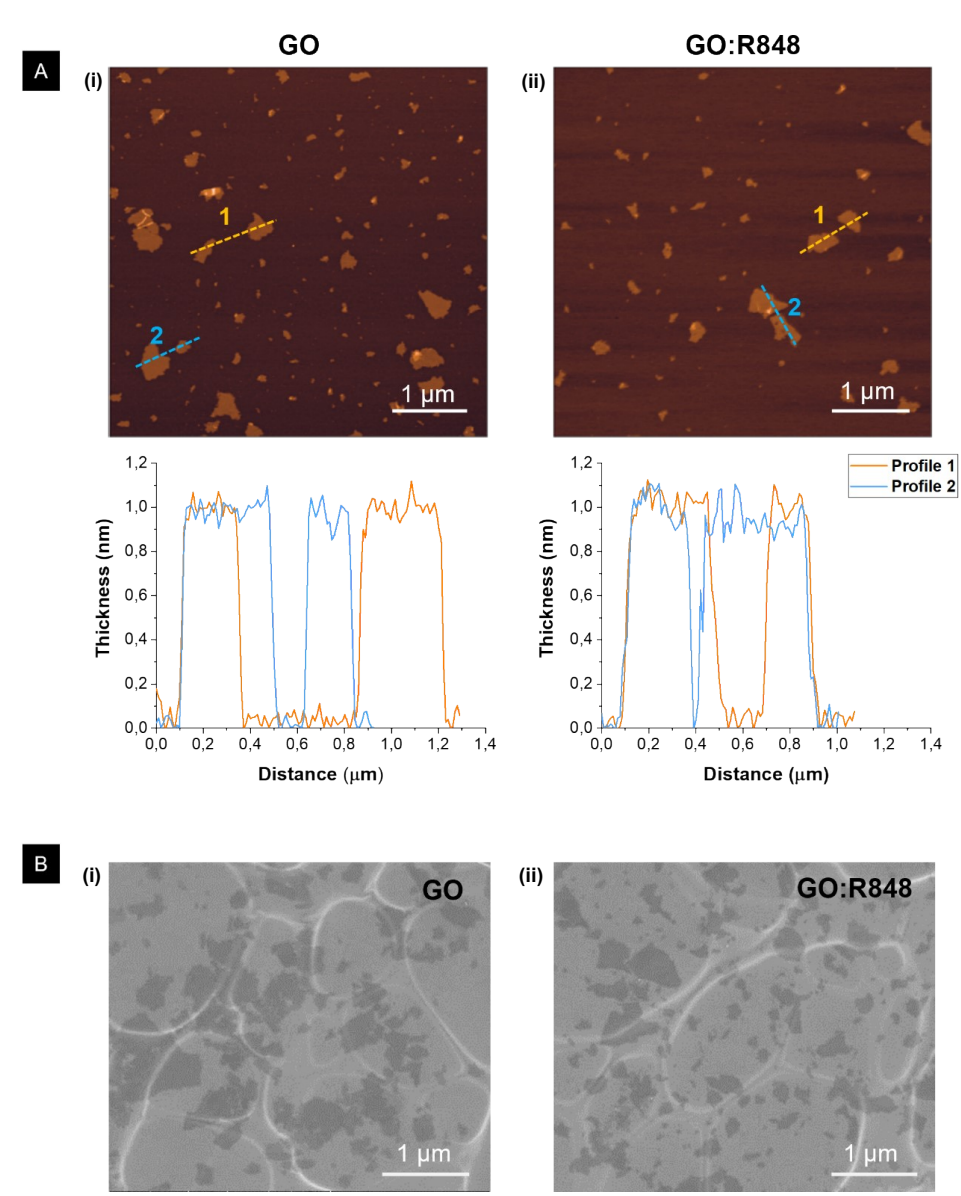


Figure 3. Morphological characterization of GO:R848 complex after purification (ap) by AFM and SEM.

(A) AFM height images with corresponding nanosheet cross-section and thickness graphs (shown underneath) of: (i) GO control; and (ii) GO:R848 complex. (B) SEM micrographs of: (i) GO control; and (ii) GO:R848 complex. In all images scale bars are 1 µm.

FIGURE 4

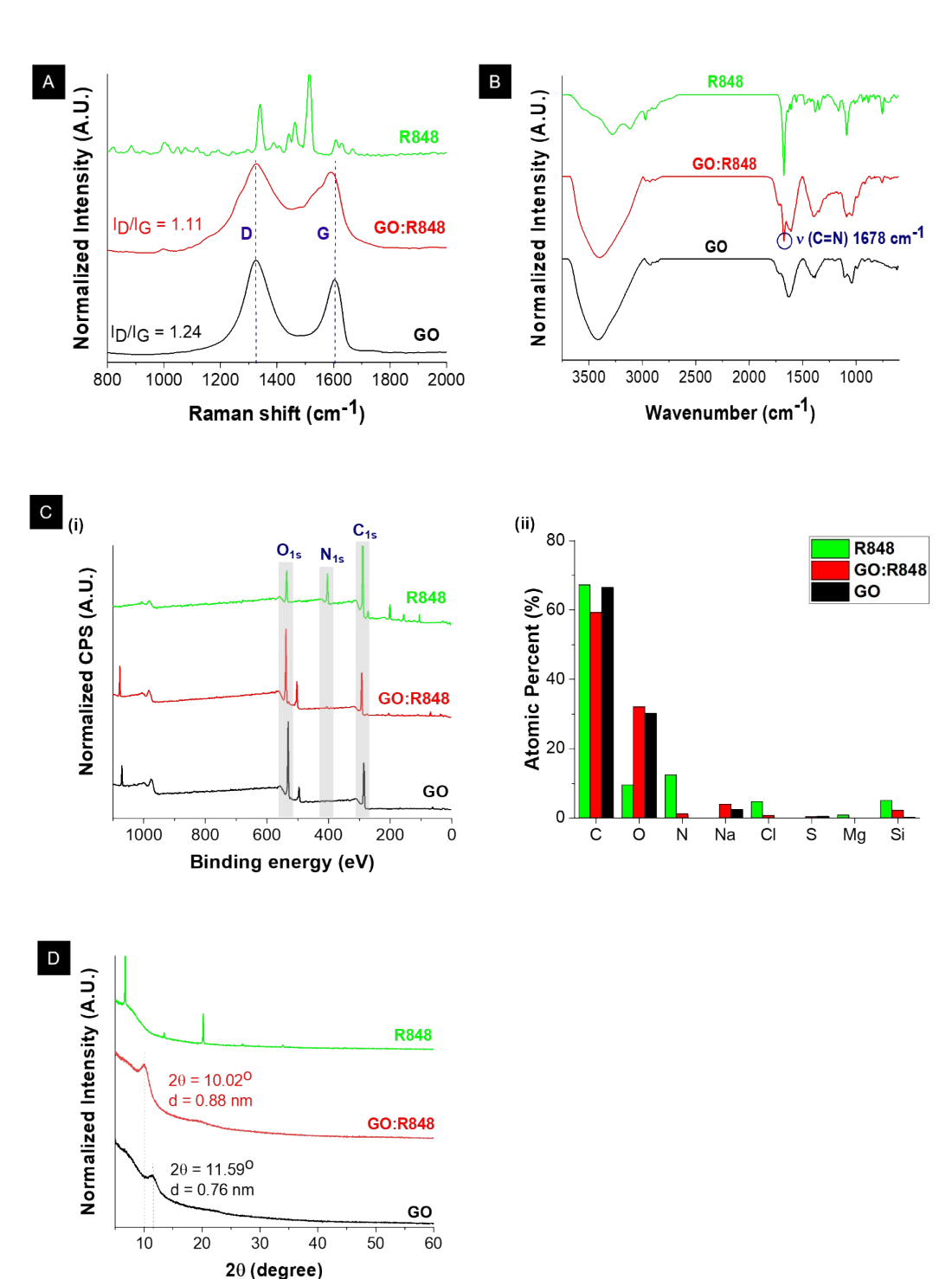


Figure 4. Spectroscopic, elemental, and structural characterization of GO:R848 complex after purification (ap).

For comparative reasons, the data for GO alone (black) and R848 alone (green) controls are also presented. (**A**) Raman spectra with the I_D and I_G bands underlined. The I_D/I_G ratios are noted. (**B**) FTIR spectra with the contribution of the characteristic surface functionality included. (**C**) (**i**) XPS high-resolution spectra with characteristic peaks of C_{1s} , O_{1s} , N_{1s} highlighted in the range of 1100-0 eV (CPS is counts per second); and (**ii**) Total contribution of various functional groups in relative atomic percentages (%) as measured by XPS. Note that the Si contribution derives from the Si substrate used during measurement. (**D**) XRD patterns with the corresponding interlayer distance highlighted. Peak intensities were generally normalized by dividing with the highest value.

This article is licensed under a Creative Commons Attribution-NonCommercial 3.0 Unported Licence.

Open Access Article. Published on 24 October 2025. Downloaded on 10/27/2025 10:14:29 AM.

FIGURE 5

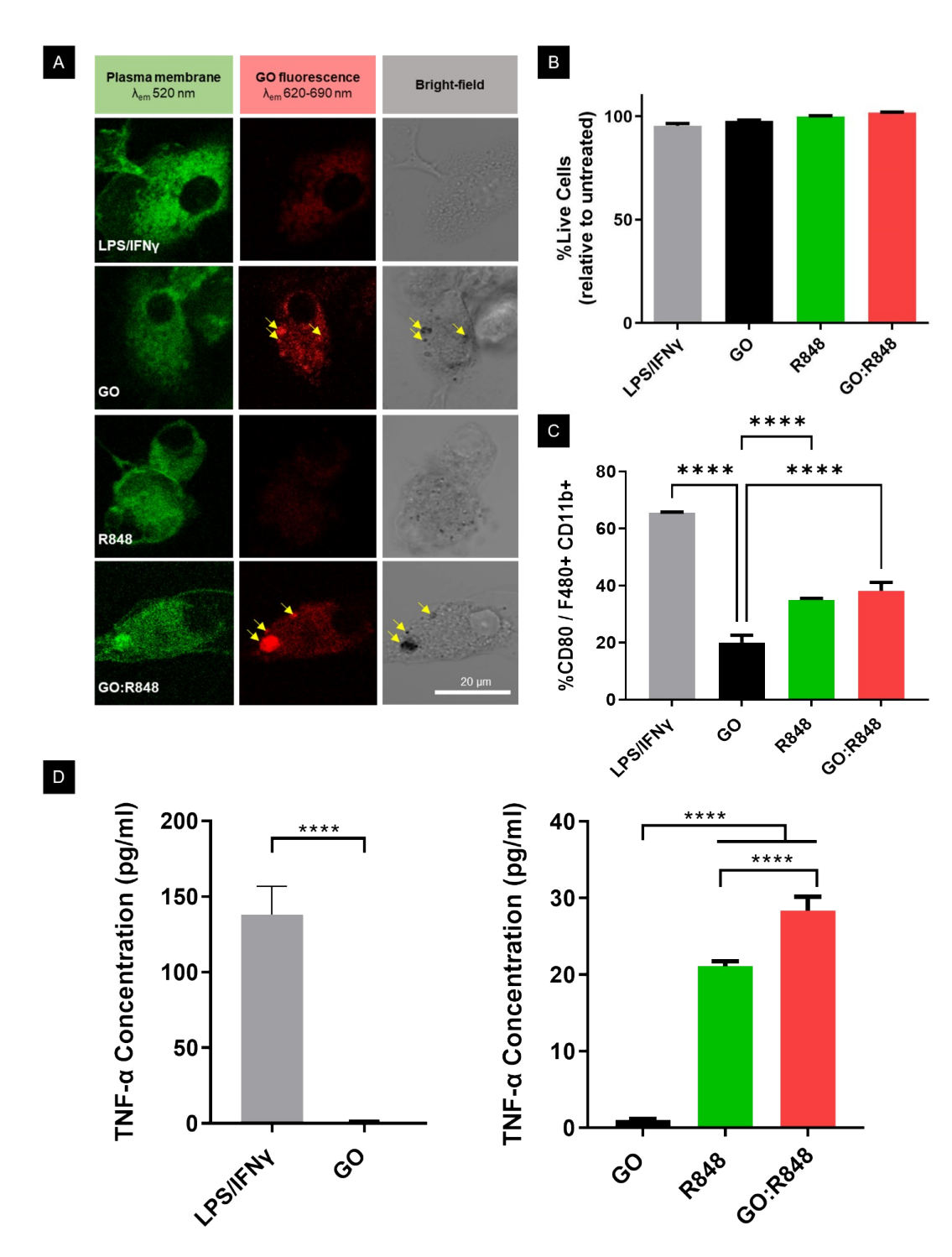


Figure 5. Biological activity of the GO:R848 complex demonstrated by effective activation of primary macrophages in vitro.

(A) Interaction of GO and GO:R848 complex with primary bone marrow-derived macrophage (BMDMs) membranes, 2 h post-treatment. Cells were stained with green plasma membrane dye. Bright field confirmed the presence of GO (black particles in bright field). GO autofluorescence (red channel) was used to detect GO-BMDMs co-localization and distinguish it from cell autofluorescence. All images were obtained with confocal microscopy at 40x magnification, zoom factor 2, scale bar 20 μ m. (B) Percentage of viable BMDMs relative to the untreated group, assessed 24 h post-treatment with LPS (100 η m/mL), GO (10 η m/mL), GO:R848 (10 η m/mL) and R848 (4 η m/mL), n= 3 biological replicates per condition. (C) Percentage of CD80 (activation marker) out of F480+ CD11b+ cells, 24 h post-treatment under the same conditions. (D) TNF- α expression (η m/ml) of BMDMs supernatant, 24 h post-treatment as mentioned above; n= 6 biological replicates per condition. Data are presented as mean \pm SD. Ordinary one-way ANOVA, Tukey's multiple comparisons test (* η p \leq 0.05, ** η p \leq 0.001, *** η p \leq 0.001, *** η p \leq 0.0001).

View Article Online DOI: 10.1039/D5TB01438G

Data availability statement

The data supporting the findings of this study have been included within the article and as part of the Supporting information.